

# Large circular photocurrent in non-centrosymmetric magnetic Weyl semimetal CeAlSi

Abhirup Roy Karmakar,<sup>1,\*</sup> A. Taraphder,<sup>1,†</sup> and G. P. Das<sup>2,‡</sup>

<sup>1</sup>*Department of Physics, Indian Institute of Technology Kharagpur, W.B. 721302, India*

<sup>2</sup>*Research Institute for Sustainable Energy (RISE), TCG Centres for Research and Education in Science and Technology, Sector V, Salt Lake, Kolkata 700091, India*

(Dated: June 7, 2025)

CeAlSi has been recently identified as a Weyl semimetal with simultaneous breaking of inversion and time-reversal symmetries. Among many potential distinguishing features that this may offer, we focus on the non-linear optical properties. We present a thorough examination of the injection current, associated with circular photogalvanic effect, from a first-principles approach. Our study demonstrates a significant injection current, exceeding previously reported results in literature. Interestingly, dominant contribution comes in the near-infrared region of the electromagnetic spectrum. In addition, we explored several externally adjustable parameters that may have a positive impact on the circular photocurrent. We uncover a substantial boost in the photocurrent through the application of uniaxial strain along  $c$ -axis of the crystal – a 5% strain results in a remarkable 62% increment. This provides insight into the exceptional optoelectronic characteristics of CeAlSi and opens up potential avenues for novel photogalvanic applications.

## I. INTRODUCTION

Weyl semimetals have captivated the condensed matter physics community, drawing considerable attention due to their distinct electronic band structure and intriguing properties. These topological materials exhibit massless Weyl fermions as fundamental quasiparticles, in contrast to the conventional solid-state physics, and inspired cutting-edge research [1–3]. The unique characteristics of Weyl semimetals (WSM) are closely linked to their symmetry-related features, making them a fascinating subject of study. In particular, Weyl semimetals break two critical symmetries in the crystal lattice: time-reversal symmetry (TRS) and inversion symmetry (IS) [4]. Time-reversal symmetry ensures the equivalence of particle dynamics when played backward in time, while inversion symmetry relates the system’s behavior under spatial inversion. The breaking of these symmetries results in the formation of pairs of Weyl points in the electronic band structure. These Weyl points act as sources and sinks of quantized Berry curvature in momentum space [5]. Additionally, the breaking of TRS in Weyl semimetals [6–10] leads to the chiral anomaly — an astounding phenomenon resulting in an imbalance of chiral fermions in the presence of parallel electric and magnetic fields. This effect gives rise to exotic transport properties such as the negative longitudinal magnetoresistance [11–13] anomalous Hall effect [14–16], anomalous thermal Hall effect [17–19], anomalous Nernst effect [18–21] etc. The other class of WSMs with broken inversion symmetry [22–30] produce another set of interesting electronic and optical phenomena like nonlinear anomalous Hall effect [31–34], second harmonic generation [35–38], bulk photovoltaic effect [39–41], circular photogalvanic effect [42–46] etc.

Among the remarkable manifestations in Weyl semimetals, the nonlinear optical properties like bulk photovoltaic effect (BPVE) and circular photogalvanic effect (CPGE) have

sparked a surge of interest and hold great promise for advancing the frontier of modern optoelectronics and photonics. The bulk photovoltaic effect manifests as a nonlinear, optically-induced charge separation within the material’s bulk, arising from the breaking of inversion symmetry. This intriguing phenomenon suggests the tantalizing potential for harnessing sunlight and transforming it into electricity in an unconventional and efficient manner [47, 48]. As we delve into the mechanisms of this effect, we uncover a treasure trove of possibilities for a sustainable and greener future. Furthermore, the circular photogalvanic effect, an engrossing manifestation of optoelectronic response unique to Weyl semimetals, unravels a dance between circularly polarized light and the chiral fermions [49–51]. This effect induces a photoinduced current resonating with the helicity of light, unlocking opportunities for innovative photonic devices and novel light manipulation techniques. It beckons us to venture into a new frontier of photonic technologies, where the collaboration of light and topological materials leads to a novel era of light-matter interactions.

To date, an array of Weyl semimetallic materials has been explored under both the symmetry classes, through experimental investigations as well as theoretical analyses. Nonetheless, the pool of systems wherein both inversion and time-reversal symmetries are concurrently broken remains limited. Notably, CeAlSi emerges as a candidate of this category, boasting noncollinear ferromagnetic order [52]. While considerable research has been devoted to studying its anomalous transport properties and Fermi arcs [52–56], the material presents numerous uncharted areas of paramount interest. In this work on CeAlSi, we present a comprehensive first-principles investigation of the injection current, a key contributor to the circular photogalvanic effect, and compare it with the shift current, which drives the bulk photovoltaic effect. Remarkably, our findings indicate a substantial magnitude of the injection current, surpassing previously reported literature results [43, 44, 57–59]. Intriguingly, it emerges as the dominant mechanism within the near-infrared region of the electromagnetic spectrum. In contrast, the contribution of the shift current remains comparatively limited with respect to the in-

\* abhirup.phy@iitkgp.ac.in

† arghya@phy.iitkgp.ac.in

‡ gour.das@tcgcrest.org

jection current. Moreover, our inquiry extends towards identifying several externally tunable parameters that positively influence the circular photocurrent. Interestingly, we observe a significant boost in the photocurrent through the application of uniaxial strain along the  $c$ -axis of the crystal. This noteworthy revelation opens new avenues for the advancement of photovoltaic technologies and underscores the material's potential in light-driven applications.

The following sections of this paper are arranged in the subsequent manner: Sec. II addresses the crystal structure, and the underlying symmetries of CeAlSi, along with an explanation of the computational methods utilized. In Sec. III, a comprehensive analysis of its intrinsic magnetization and electronic structure is conducted. Sec. IV presents the theory and outcomes related to shift current and injection current. Subsequently, Sec. V explores the impact of magnetic ordering and stress on the circular photocurrent and how it leads to enhancement. Finally, in Sec. VI, we offer a summary of our work and potential future research directions.

## II. MATERIAL AND METHOD

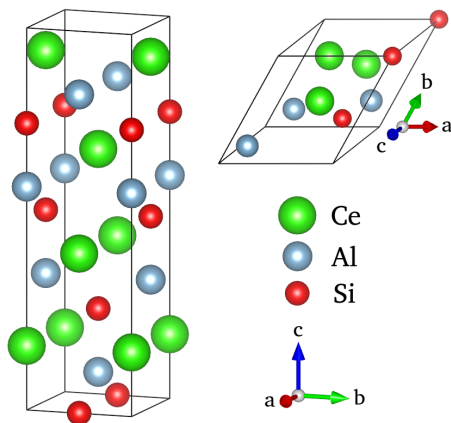


FIG. 1: **Crystal structure of CeAlSi.** The left part of the figure shows the tetragonal structure of the conventional unit cell (space group  $I4_1md$ ). The primitive cell of the system is shown on the right along with its lattice vectors.

CeAlSi has a noncentrosymmetrically ordered structure with a space group of  $I4_1md$  (No. 109) and is an isostructure of CeAlGe which was first proposed as a Ferromagnetic Weyl semimetal [60, 61]. The tetragonal unit cell has the experimental lattice parameters  $a = 4.25 \text{ \AA}$  and  $c = 14.58 \text{ \AA}$ . Although this crystal structure of point group  $4mm$  possesses a four-fold rotation axis ( $C_{4v}$ ) and two vertical mirror planes ( $\sigma_v$ ), it lacks the horizontal mirror plane ( $\sigma_h$ ) which is responsible for the breaking of inversion symmetry. On another note, site-mixing between the elements Al and Si could restore the horizontal mirror plane ( $\sigma_h$ ) and thereby transforming the structure into a centrosymmetric one with space group  $I4_1/amd$ . However, people have confirmed the structure to be  $I4_1md$  by measuring second-harmonic generation (SHG)

which only occurs in non-centrosymmetric systems [52].

We have performed first principles density functional theory (DFT) calculations using Vienna Ab initio Simulation Package (VASP) [62] in the projector augmented wave (PAW) approximation. Generalized gradient approximation (GGA) was considered for exchange-correlation functional in the Perdew-Burke-Ernzerhof (PBE) scheme [63]. A  $15 \times 15 \times 15$  Monk-horst grid was taken to fill the 3D Brillouin zone. To account for the  $f$ -electrons of Ce atoms, an on-site Coulomb interaction of strength  $U_{eff} = 7 \text{ eV}$  was added within the approach given by Dudarev *et al.* [64]. We projected the Bloch wave functions obtained from this DFT+U calculation into the maximally localized Wannier functions (MLWFs) and obtained Hamiltonian matrix elements between the MLWFs with the help of Wannier90 package [65]. The  $d$ -orbitals of Ce and  $s, p$ -orbitals of Al and Si have been chosen as the projections for the Wannierization. In order for a thorough investigation of the band structure and calculation of the photocurrents, we derived a Hamiltonian using the Wannier tight-binding model with 52 bands from the matrix elements [65, 66]. All other numerical calculations were performed in Python programming language and with the help of WannierBerri [67] package.

## III. ELECTRONIC STRUCTURE

To start with, we plotted the orbital-projected density of states (PDOS) in Fig. 2a. Different colors corresponds to different orbitals as mentioned in the legend and positive and negative parts correspond to the spin-up and spin-down channels respectively. It is clearly visible that the  $f$ -orbital of Ce peaks out the most and there is a significant asymmetry between the two spin channels. This dictates the magnetic nature of the system which predominantly comes only from the Ce- $f$  orbitals. The inset figure of PDOS is the zoomed-in version of the former one and gives us two important information: (i) at energy levels close to the Fermi level ( $\epsilon_F$ ), only the  $d$ -orbital of Ce atoms dominate and the rest including Ce- $f$  have negligible contribution. (ii) PDOS is symmetric near  $\epsilon_F$  which implies that the magnetization of the system is very localized and away from  $\epsilon_F$ . Since the unit cell has element with large atomic number, it is customary to incorporate spin-orbit coupling (SOC). Upon performing the DFT calculation including SOC, we found that the system has a noncollinear Ferromagnetic order with net magnetization vector [1.1, 1.1, 0.3]. The individual Ce atoms in the unit cell, i.e. the major contributor to magnetization, has a magnetic moment of  $0.89 \mu_B$ . Now, to gain more insight of the electronic structure, we plotted the band structure in Fig. 2c along the high-symmetry path  $\Gamma - \Sigma - N - \Sigma_1 - Z - \Gamma - X$  in the Brillouin zone as shown in Fig. 2b(i). The band-splittings are clearly visible in the plot which are caused by the effect of SOC. By observing the red lines representing the valence and conduction bands, one can see two band crossings around the high-symmetry points  $\Sigma$  and one along the direction  $N - \Sigma_1$ . However, by scanning throughout the Brillouin zone in three-dimensional reciprocal space, we obtained 20 pairs of Weyl nodes in total. These are all plotted in Fig. 2b(ii) with different colors as per their lo-

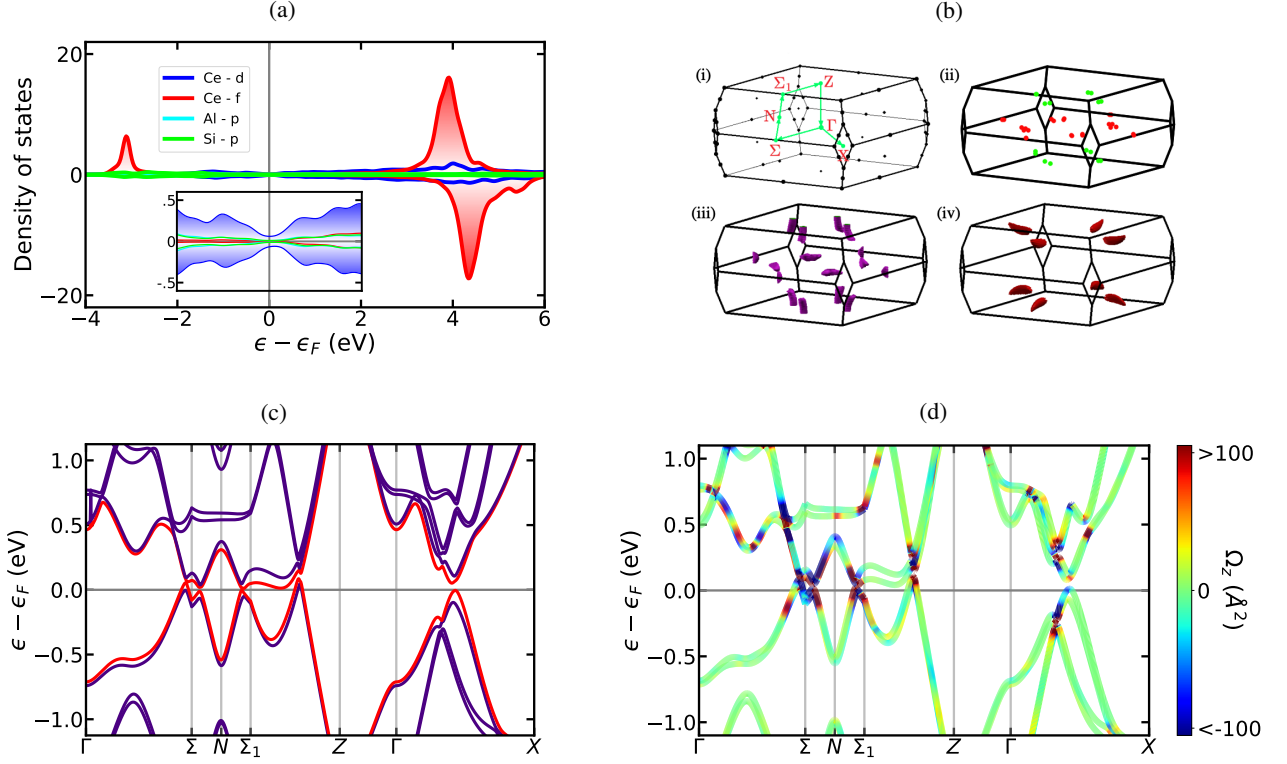


**FIG. 2: Electronic structure of CeAlSi.** (a) The orbital-projected density of states. The asymmetry in the large peaks of the red curve (Ce- $f$  orbital) indicates the magnetic nature of the system. However, the  $f$ -orbital does not have much dominance near Fermi level as depicted in the inset figure. The +ve and -ve values correspond to spin-up and spin-down channels respectively. (b) (i): Brillouin zone of the unit cell where the green line indicates the high-symmetry path for band structure. (ii): Locations of the Weyl nodes inside the Brillouin zone. Red dots are the nodes lying on the  $k_z = 0$  plane, whereas green dots correspond to the rest. (iii) and (iv): Fermi surfaces of valence (purple) and conduction bands (red) respectively. This demonstrates that the valence band crosses the Fermi level in the Brillouin zone more frequently than the conduction band. (c) The band structure with spin-orbit coupling is plotted along the high symmetry direction  $\Gamma - \Sigma - N - \Sigma_1 - Z - \Gamma - X$ . The valence and the conduction bands are colored in red. (d) Berry curvature resolved band structure along the high-symmetry path. The color coding represents the values of the  $z$ -component of Berry curvature as shown in the color bar.

cations. Twelve pairs of them lie at the  $k_y = 0$  plane while eight other pairs are located away from the plane. The Weyl nodes are situated at various energy levels ranging from 0 to 110 meV with respect to the Fermi level due to broken inversion symmetry. The Fermi surfaces for valence and conduction bands are plotted in 2b(iii)-(iv). It is clear that the valence band crosses  $\epsilon_F$  more often than conduction band. The figures illustrate the hole and electron pockets confirming the negligible density of states near  $\epsilon_F$ . The residual hole pockets are also consistent with Fig. 2b(ii) in terms of the locations of the nodes.

#### IV. NONLINEAR PHOTOCURRENTS

Circular photogalvanic effect is the phenomenon where circularly polarized light incident on a material induces a time-dependent current density that manifests in a DC current response. Whereas, the bulk photovoltaic effect is a DC current

response due to linearly polarized light. Although these two effects can be produced by various mechanisms, we focus here only on the second-order intrinsic contributions, namely the “shift current” and “injection current” for BPVE and CPGE, respectively. The total nonlinear photocurrent density in terms of the two can be written as,

$$\langle \mathbf{J}_{DC} \rangle^{(2)} = \langle \mathbf{J}_{SC} \rangle^{(2)} + \langle \mathbf{J}_{IC} \rangle^{(2)} \quad (1)$$

where,

$$\begin{aligned} \langle \mathbf{J}_{SC}^a \rangle^{(2)} &= \sigma_2^{abc}(0; \omega, -\omega) \mathbf{E}^b(\omega) \mathbf{E}^c(-\omega) \\ \frac{d}{dt} \langle \mathbf{J}_{IC}^a \rangle^{(2)} &= \eta_2^{abc}(0; \omega, -\omega) \mathbf{E}^b(\omega) \mathbf{E}^c(-\omega) \end{aligned}$$

with  $a, b, c$  being the cartesian indices;  $\sigma_2^{abc}$  and  $\eta_2^{abc}$  are respectively the shift-current and injection current susceptibility tensor. The electric fields  $\mathbf{E}(\omega)$  are real in case of linearly polarized light, whereas they are complex for circularly polarized light. The photocurrent tensors can be mathematically

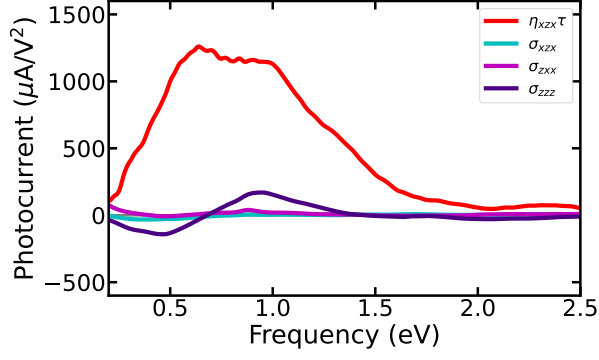


FIG. 3: Injection current and shift currents are plotted as a function of incident light frequency for  $\frac{\hbar}{\tau} = 20$  meV.  $\eta\tau$  is the maximum value of  $1260 \mu\text{A}/\text{V}^2$  and is dominant throughout a broad region in the infrared spectrum with two peaks located at 0.64 and 0.99 eV. On the other hand, shift current values remain well below the above mentioned value of injection current and has two peaks at 0.47 eV and 0.94 eV.

calculated using the following expressions [68]

$$\sigma_2^{abc} = -\frac{i\pi e^3}{2\hbar^2} \int \frac{d\mathbf{k}}{(2\pi)^3} \sum_{n,m} f_{nm} (r_{mn}^b r_{nm;a}^c + r_{mn}^c r_{nm;a}^b) \times \delta(\epsilon_{mn} - \hbar\omega) \quad (2)$$

$$\eta_2^{abc} = \frac{\pi e^3}{2\hbar^2} \int \frac{d\mathbf{k}}{(2\pi)^3} \sum_{n,m} \Delta_{mn}^a f_{nm} (r_{mn}^b r_{nm}^c - r_{mn}^c r_{nm}^b) \times \delta(\epsilon_{mn} - \hbar\omega) \quad (3)$$

where,  $m, n$  are the band indices.  $\epsilon_{mn} = \epsilon_m - \epsilon_n$ ,  $f_{mn} = f_m - f_n$  are the differences of band energies and Fermi-Dirac occupation number respectively.  $\Delta_{mn}^a = \partial_{k_a} \epsilon_{mn}$ ,  $r_{mn}^a = A_{mn}^a = i\langle m | \partial_{k_a} | n \rangle$  ( $m \neq n$ ) is the interband matrix element (off-diagonal Berry connection), and  $r_{nm;a}^b = \partial_{k_a} r_{mn}^b - i(A_{nn}^a - A_{mm}^a) r_{mn}^b$  is the generalized derivative of the matrix element. For numerical evaluation of Eq. (3), we replace delta function with the Lorentzian function  $\frac{1}{\pi} \frac{\Gamma}{(\epsilon_{mn} - \hbar\omega)^2 + \Gamma^2}$ , where  $\Gamma = \hbar/\tau$  ( $\tau$  is the relaxation time).

For a two-band model system, the above equation takes the form [58]

$$\eta_2^{abc} = \frac{i\pi e^3}{2\hbar^2} \int \frac{d\mathbf{k}}{(2\pi)^3} \Delta_{12}^a \Omega_v^{bc} \times \delta(\epsilon_{21} - \hbar\omega) \quad (4)$$

where 1,2 correspond to valence and conduction bands respectively, and  $\Omega_v^{bc}$  is the valence band Berry curvature. Although, in this work we are dealing with a realistic material with 52 bands, it is important to understand from Eq. (3) that all the interband transitions counted are between two bands  $m$  and  $n$ . And hence, having non-zero values of Berry curvature for the bands will give us a hint towards getting a finite value injection current. In Fig. 2d, we plot the Berry curvature resolved band

structure of the system where we demonstrate the finiteness of the curvature for each band near Fermi level along the high symmetry k-path. The color coding is for  $z$ -component of the quantity, which is clearly explained in the color bar outside.

For this particular crystal class, the non-zero susceptibility tensor elements are  $xzx = yzy$ ,  $xzx = yzy$ ,  $zxx = zyy$  and  $zzz$  [69]. However, according to the equations (2), (3) and ref. [68],  $\sigma_2^{xzx} = \sigma_2^{xzz}$ ,  $\eta_2^{xzx} = -\eta_2^{xzz}$  and  $\eta_2^{zxx} = \eta_2^{zzz} = 0$ . So, the only independent non-zero elements are  $\sigma_2^{xzx}$ ,  $\sigma_2^{zxx}$ ,  $\sigma_2^{zzz}$  and  $\eta_2^{xzx}$ . The first index represents the direction of photocurrent and the last two represent the polarization of light. Hence, shift current is generated by both linearly-polarized ( $\sigma_2^{zxx}$ ,  $\sigma_2^{zzz}$ ) as well as circularly-polarized ( $\sigma_2^{xzx}$ ) light, whereas injection current can only be produced by circularly-polarized light.

Since, the photocurrent tensors are obtained from transitions between multiple bands (both real and virtual), they are heavily dependent on the incident light frequency. Also, relaxation time plays a major role in the photocurrent calculation, especially for injection current. For a typical metallic system  $\frac{\hbar}{\tau}$  should be of the order of  $k_B T$ . Here, we do our calculations in room temperature ( $T = 300$  K) and accordingly choose  $\frac{\hbar}{\tau} = 20$  meV ( $\tau \sim 33$  fs). The independent injection current component along with the non-zero shift currents are plotted in Fig. 3. It is quite interesting that the circular photocurrent attains large values for a wide range in the infrared spectrum with a maximum of  $1260 \mu\text{A}/\text{V}^2$ . The two visible peaks are situated at 0.64 and 0.99 eV which correspond to 1940 nm and 1250 nm respectively, falling in the near-infrared (NIR) region (2526 – 780 nm). If we calculate the full width at half maximum (FWHM),  $\eta_{xzx}$  turns out to be dominant in the range 0.39 – 1.29 eV (3180 – 961 nm). As compared to the values of injection current, shift current does not exhibit much contribution in the system. The largest component  $\sigma_{zzz}$  attains up to  $170 \mu\text{A}/\text{V}^2$  at around 0.94 eV and has another negative peak at 0.47 eV. In the next section, we do further analysis of  $\eta_{xzx}$  in terms of external factors.

## V. EXTERNAL INFLUENCES

In this section we look for the externally tunable parameters that can increase the amount of photocurrent. Motivated by the work of Alam *et al.* [53], we study CPGE for two different magnetic configurations. In its ground state, CeAlSi has noncollinear magnetic order with moments directed between  $a$ -axis and  $b$ -axis on  $ab$ -plane. We calculate injection current for two cases of collinear magnetization: (i) magnetic moments along  $a$ -axis and (ii) magnetic moments along  $c$ -axis. It turns out that when magnetization is along  $a$ -axis, peak of the photocurrent profile remains almost similar to that of the ground state with noncollinear order. However, when the moments are forced to align towards the hard axis ( $c$ -axis), the peak value increases by a small amount. The peak now shifts to the center of the plateau region and all the values in that region get enhanced. To be quantitative, the peak goes from  $1260 \mu\text{A}/\text{V}^2$  to  $1320 \mu\text{A}/\text{V}^2$ .

To account for another external influence, we choose strain

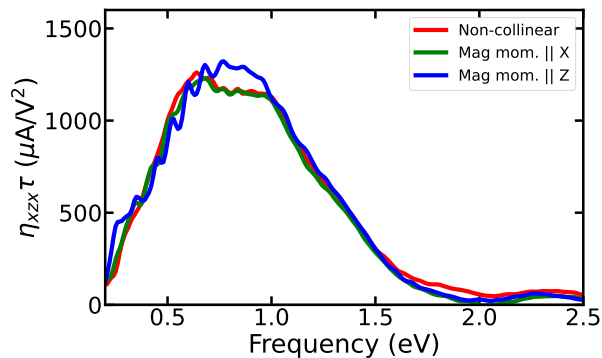


FIG. 4: Injection current plotted for different orientations of magnetic moments. The photocurrent profile for magnetization along  $a$ -axis (green) is almost similar to that of the pristine (red). However, it increases a little when magnetization is along  $c$ -axis (blue). The plateau region also peaks out at its center and consequently shifts the initial peak position.

as the parameter. Similar to previous case, we investigate two kinds of compressive strain: (i) along  $a$ -axis and (ii) along  $c$ -axis. In the case of (i), we observe a decrease in the magnitude of  $\eta_{xzx}$ . Whereas, applying compressive stress along the  $c$ -axis drastically improves the circular photogalvanic effect. The maximum value of  $\eta_{xzx}$  goes up by 62% from the pristine value at 5% strain corresponding to a stress of 10.4 GPa; which implies a huge current response of  $2040 \mu\text{A}/\text{V}^2$  (Fig. 5). Not only that, the plateau region of the red curve gets sharpened gradually with the application of stress and the peak gets centered in the FWHM region. This leads to a shift of the peak frequency from 0.64 eV to 0.77 eV for a stress of 10.4 GPa.

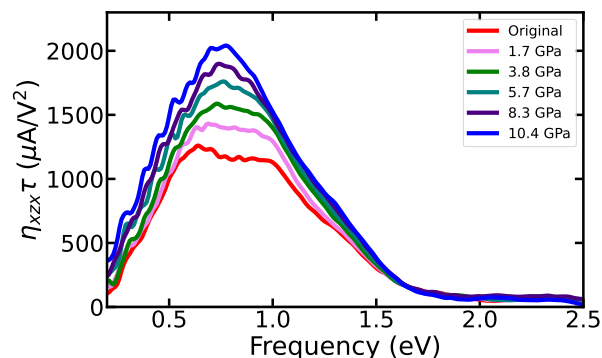


FIG. 5: The multicolored curves represent injection current for different amounts of compressive stress along  $c$ -axis. The values increase and the plateau region gradually peaks out at center with increasing stress. The maximum value reaches to  $2040 \mu\text{A}/\text{V}^2$  with an increment of 62% at a stress of 10.4 GPa (blue) from the ground state (red).

To understand this effect of strain on CPGE we closely analyze the behavior of electronic structure under strain since the injection current is after all due to the interaction between the

bands as seen in Eq. (3). In Fig. 6, we plot the band structures (upper row) and the Weyl node-energies (lower row) for various amounts of stress. With increasing stress, the valence and conduction bands shift towards higher energies along the high-symmetry paths  $\Gamma - \Sigma$  and  $\Gamma - X$  which goes through the bulk Brillouin zone. For instance, the valence band peak along  $\Gamma - X$  stays at the Fermi level in absence of stress. However, at higher stresses, the peak goes up significantly from the Fermi level as shown in Figs. 6(a-c). The same behavior is seen for conduction band as well the above mentioned paths. A different picture is coming out when observing the bands along the path  $\Sigma - N - \Sigma_1 - Z$  lying on the outer surface of the Brillouin zone. In this case, the valence and conduction band energies decrease with respect to Fermi level when the stress is increased. This is also easily observed in Figs. 6(a-c) by focusing on the crests and troughs of the bands. In other words, the energy differences between the bands change inhomogeneously throughout the Brillouin zone in presence of stress. Consequently, the integration of the two-band quantities in Eq. (3) throughout the momentum space changes. Another interesting thing to look at is the distribution of Weyl nodes Figs. 6(d-f). The system in its ground state holds 20 pairs of nodes with opposite chirality having energy up to 110 meV. At 5.7 GPa stress, the nodes scatter more in energy scale and remain between  $-50$  to 180 meV. Interestingly, increasing stress beyond this point creates more Weyl points and at a stress of 10.4 GPa, there are 56 nodes in total scattered between  $-100$  and 250 meV. This is due to inhomogeneous shifting of the bands as we have explained above.

## VI. SUMMARY

We have presented our findings on nonlinear photocurrents in the noncentrosymmetric WSM CeAlSi induced by both linearly and circularly polarized light, using a multi-band approach, derived from the first-principles calculations. Our study commenced with a comprehensive investigation of the electronic structure of CeAlSi, wherein we observed that the noncollinear ferromagnetic nature of the material and thereby breaking of time-reversal symmetry is attributed to the  $f$ -electron in the Ce atom. We identified 20 pairs of Weyl nodes spanning an energy range of 0 to 110 meV. On integration of relevant quantities as described in equations (2) and (3) across 52 bands throughout the Brillouin zone, we were able to determine both the shift current responsible for the bulk photovoltaic effect, as well as the injection current driving the circular photogalvanic effect. The results implied that the system exhibits a large amount of injection current on irradiation of light compared to the shift current. Notably, the dominant portion of the injection photocurrent is located within the near-infrared (NIR) region of the electromagnetic spectrum. Additionally, we explored various external parameters to modulate the intrinsic photocurrent response. Our findings indicate that a uniaxial compressive strain along the  $c$ -axis gives a significant enhancement of the photocurrent. For instance, the application of a stress of 10.4 GPa resulted in a remarkable 62% increase in the injection current compared to the value in the

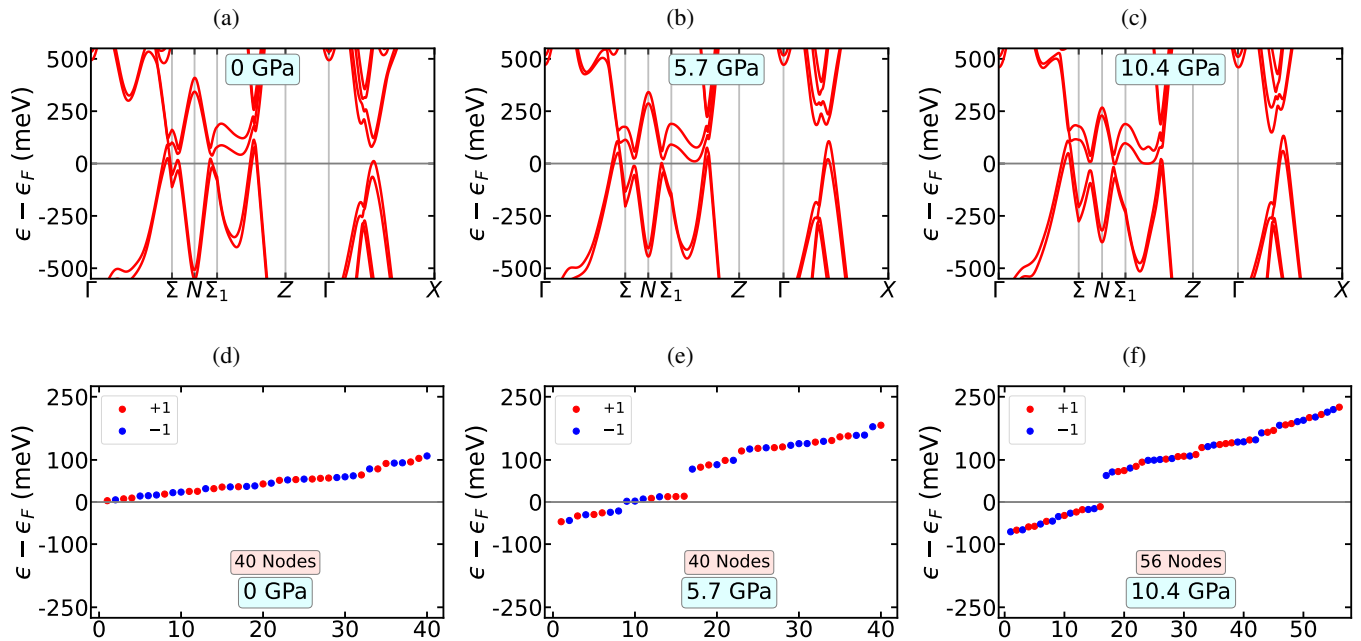


FIG. 6: **Strain-induced band dispersion and Weyl node energies.** (a)-(c) Band structures with SOC for different amounts of uniaxial compressive stress along  $c$ -axis. The energy of the valence and conduction bands increases with stress along the paths  $\Gamma - \Sigma$  and  $\Gamma - X$  which are inside the Brillouin zone. However, the band energies decrease along the path  $\Sigma - N - \Sigma_1 - Z$  which lie on the outer surface of the Brillouin zone. (d)-(f) The Weyl nodes are plotted in energy scale and marked their chiralities with distinct colors (*red* and *blue*). The spread in energy increases with increasing stress and goes from 0 – 110 meV to a range between –100 and 180 meV. Moreover, the number of nodes increases to 40 to 56 at a stress of 10.4 GPa.

ground state. In conclusion, our work suggests that the Weyl semimetal CeAlSi holds great promise as a renewable energy source, contributing positively to environmental sustainability.

#### ACKNOWLEDGMENTS

A.R.K. acknowledges IIT Kharagpur for a research fellowship and National Supercomputing Mission (NSM) for providing computing resources of “PARAM Shakti” at IIT Kharagpur, which is implemented by C-DAC and supported by the Ministry of Electronics and Information Technology (MeitY) and Department of Science and Technology (DST), Government of India.

- 
- [1] N. P. Armitage, E. J. Mele, and A. Vishwanath, Weyl and Dirac semimetals in three-dimensional solids, *Rev. Mod. Phys.* **90**, 015001 (2018).
- [2] A. Bansil, H. Lin, and T. Das, *Colloquium* : Topological band theory, *Rev. Mod. Phys.* **88**, 021004 (2016).
- [3] B. Yan and C. Felser, Topological Materials: Weyl Semimetals, *Annu. Rev. Condens. Matter Phys.* **8**, 337 (2017).
- [4] A. A. Zyuzin, S. Wu, and A. A. Burkov, Weyl semimetal with broken time reversal and inversion symmetries, *Phys. Rev. B* **85**, 165110 (2012).
- [5] D. Xiao, M.-C. Chang, and Q. Niu, Berry phase effects on electronic properties, *Rev. Mod. Phys.* **82**, 1959 (2010).
- [6] X. Wan, A. M. Turner, A. Vishwanath, and S. Y. Savrasov, Topological semimetal and Fermi-arc surface states in the electronic structure of pyrochlore iridates, *Phys. Rev. B* **83**, 205101 (2011).
- [7] K.-Y. Yang, Y.-M. Lu, and Y. Ran, Quantum Hall effects in a Weyl semimetal: Possible application in pyrochlore iridates, *Phys. Rev. B* **84**, 075129 (2011).
- [8] J. Ruan, S.-K. Jian, D. Zhang, H. Yao, H. Zhang, S.-C. Zhang, and D. Xing, Ideal Weyl Semimetals in the Chalcopyrites CuTlSe<sub>2</sub>, AgTlTe<sub>2</sub>, AuTlTe<sub>2</sub>, and ZnPbAs<sub>2</sub>, *Phys. Rev. Lett.* **116**, 226801 (2016).
- [9] G. Chang, B. J. Wieder, F. Schindler, D. S. Sanchez, I. Belopolski, S.-M. Huang, B. Singh, D. Wu, T.-R. Chang, T. Neupert, S.-Y. Xu, H. Lin, and M. Z. Hasan, Topological quantum properties of chiral crystals, *Nature Mater* **17**, 978 (2018).
- [10] A. Roy Karmakar, S. Nandy, G. P. Das, and K. Saha, Probing mirror anomaly and classes of Dirac semimetals with circular dichroism, *Phys. Rev. Research* **3**, 013230 (2021).
- [11] X. Huang, L. Zhao, Y. Long, P. Wang, D. Chen, Z. Yang, H. Liang, M. Xue, H. Weng, Z. Fang, X. Dai, and G. Chen, Ob-

- servation of the Chiral-Anomaly-Induced Negative Magnetoresistance in 3D Weyl Semimetal TaAs, *Phys. Rev. X* **5**, 031023 (2015).
- [12] F. Arnold, C. Shekhar, S.-C. Wu, Y. Sun, R. D. Dos Reis, N. Kumar, M. Naumann, M. O. Ajeesh, M. Schmidt, A. G. Grushin, J. H. Bardarson, M. Baenitz, D. Sokolov, H. Borrmann, M. Nicklas, C. Felser, E. Hassinger, and B. Yan, Negative magnetoresistance without well-defined chirality in the Weyl semimetal TaP, *Nat Commun* **7**, 11615 (2016).
- [13] Y. Wang, E. Liu, H. Liu, Y. Pan, L. Zhang, J. Zeng, Y. Fu, M. Wang, K. Xu, Z. Huang, Z. Wang, H.-Z. Lu, D. Xing, B. Wang, X. Wan, and F. Miao, Gate-tunable negative longitudinal magnetoresistance in the predicted type-II Weyl semimetal WTe<sub>2</sub>, *Nat Commun* **7**, 13142 (2016).
- [14] A. A. Burkov, Anomalous Hall Effect in Weyl Metals, *Phys. Rev. Lett.* **113**, 187202 (2014).
- [15] J. F. Steiner, A. V. Andreev, and D. A. Pesin, Anomalous Hall Effect in Type-I Weyl Metals, *Phys. Rev. Lett.* **119**, 036601 (2017).
- [16] C. Shekhar, N. Kumar, V. Grinenko, S. Singh, R. Sarkar, H. Luetkens, S.-C. Wu, Y. Zhang, A. C. Komarek, E. Kampert, Y. Skourski, J. Wosnitza, W. Schnelle, A. McCollam, U. Zeitler, J. Kübler, B. Yan, H.-H. Klauss, S. S. P. Parkin, and C. Felser, Anomalous Hall effect in Weyl semimetal half-Heusler compounds RPtBi (R = Gd and Nd), *Proc. Natl. Acad. Sci. U.S.A.* **115**, 9140 (2018).
- [17] A. Roy Karmakar, S. Nandy, A. Taraphder, and G. P. Das, Giant anomalous thermal Hall effect in tilted type-I magnetic Weyl semimetal Co<sub>3</sub>Sn<sub>2</sub>S<sub>2</sub>, *Phys. Rev. B* **106**, 245133 (2022).
- [18] E. V. Gorbar, V. A. Miransky, I. A. Shovkovy, and P. O. Sukhachov, Anomalous thermoelectric phenomena in lattice models of multi-Weyl semimetals, *Phys. Rev. B* **96**, 155138 (2017).
- [19] Y. Ferreira, A. A. Zyuzin, and J. H. Bardarson, Anomalous Nernst and thermal Hall effects in tilted Weyl semimetals, *Phys. Rev. B* **96**, 115202 (2017).
- [20] S. J. Watzman, T. M. McCormick, C. Shekhar, S.-C. Wu, Y. Sun, A. Prakash, C. Felser, N. Trivedi, and J. P. Heremans, Dirac dispersion generates unusually large Nernst effect in Weyl semimetals, *Phys. Rev. B* **97**, 161404 (2018).
- [21] F. Cagliaris, C. Wuttke, S. Sykora, V. Süss, C. Shekhar, C. Felser, B. Büchner, and C. Hess, Anomalous Nernst effect and field-induced Lifshitz transition in the Weyl semimetals TaP and TaAs, *Phys. Rev. B* **98**, 201107 (2018).
- [22] B. Q. Lv, N. Xu, H. M. Weng, J. Z. Ma, P. Richard, X. C. Huang, L. X. Zhao, G. F. Chen, C. E. Matt, F. Bisti, V. N. Strocov, J. Mesot, Z. Fang, X. Dai, T. Qian, M. Shi, and H. Ding, Observation of Weyl nodes in TaAs, *Nature Phys* **11**, 724 (2015).
- [23] S.-Y. Xu, I. Belopolski, D. S. Sanchez, C. Zhang, G. Chang, C. Guo, G. Bian, Z. Yuan, H. Lu, T.-R. Chang, P. P. Shibayev, M. L. Prokopovych, N. Alidoust, H. Zheng, C.-C. Lee, S.-M. Huang, R. Sankar, F. Chou, C.-H. Hsu, H.-T. Jeng, A. Bansil, T. Neupert, V. N. Strocov, H. Lin, S. Jia, and M. Z. Hasan, Experimental discovery of a topological Weyl semimetal state in TaP, *Sci. Adv.* **1**, e1501092 (2015).
- [24] S.-Y. Xu, I. Belopolski, N. Alidoust, M. Neupane, G. Bian, C. Zhang, H. Sankar, G. Chang, Z. Yuan, C.-C. Lee, S.-M. Huang, H. Zheng, J. Ma, D. S. Sanchez, B. Wang, A. Bansil, F. Chou, P. P. Shibayev, H. Lin, S. Jia, and M. Zahid Hasan, Discovery of a Weyl fermion semimetal and topological Fermi arcs, *Science* **349**, 613 (2015).
- [25] S.-Y. Xu, N. Alidoust, I. Belopolski, Z. Yuan, G. Bian, T.-R. Chang, H. Zheng, V. N. Strocov, D. S. Sanchez, G. Chang, C. Zhang, D. Mou, Y. Wu, L. Huang, C.-C. Lee, S.-M. Huang, B. Wang, A. Bansil, H.-T. Jeng, T. Neupert, A. Kaminski, H. Lin, S. Jia, and M. Zahid Hasan, Discovery of a Weyl fermion state with Fermi arcs in niobium arsenide, *Nature Phys* **11**, 748 (2015).
- [26] S.-M. Huang, S.-Y. Xu, I. Belopolski, C.-C. Lee, G. Chang, B. Wang, N. Alidoust, G. Bian, M. Neupane, C. Zhang, S. Jia, A. Bansil, H. Lin, and M. Z. Hasan, A Weyl Fermion semimetal with surface Fermi arcs in the transition metal monophenictide TaAs class, *Nat Commun* **6**, 7373 (2015).
- [27] H. Weng, C. Fang, Z. Fang, B. A. Bernevig, and X. Dai, Weyl Semimetal Phase in Noncentrosymmetric Transition-Metal Monophosphides, *Phys. Rev. X* **5**, 011029 (2015).
- [28] L. Lu, Z. Wang, D. Ye, L. Ran, L. Fu, J. D. Joannopoulos, and M. Soljačić, Experimental observation of Weyl points, *Science* **349**, 622 (2015).
- [29] N. Xu, H. M. Weng, B. Q. Lv, C. E. Matt, J. Park, F. Bisti, V. N. Strocov, D. Gawryluk, E. Pomjakushina, K. Conder, N. C. Plumb, M. Radovic, G. Autès, O. V. Yazyev, Z. Fang, X. Dai, T. Qian, J. Mesot, H. Ding, and M. Shi, Observation of Weyl nodes and Fermi arcs in tantalum phosphide, *Nat Commun* **7**, 11006 (2016).
- [30] U. Dey, S. Nandy, and A. Taraphder, Dynamic chiral magnetic effect and anisotropic natural optical activity of tilted Weyl semimetals, *Sci Rep* **10**, 2699 (2020).
- [31] I. Sodemann and L. Fu, Quantum Nonlinear Hall Effect Induced by Berry Curvature Dipole in Time-Reversal Invariant Materials, *Phys. Rev. Lett.* **115**, 216806 (2015).
- [32] R.-H. Li, O. G. Heinonen, A. A. Burkov, and S. S.-L. Zhang, Nonlinear Hall effect in Weyl semimetals induced by chiral anomaly, *Phys. Rev. B* **103**, 045105 (2021).
- [33] D. Kumar, C.-H. Hsu, R. Sharma, T.-R. Chang, P. Yu, J. Wang, G. Eda, G. Liang, and H. Yang, Room-temperature nonlinear Hall effect and wireless radiofrequency rectification in Weyl semimetal TaIrTe<sub>4</sub>, *Nat. Nanotechnol.* **16**, 421 (2021).
- [34] C. Zeng, S. Nandy, and S. Tewari, Nonlinear transport in Weyl semimetals induced by Berry curvature dipole, *Phys. Rev. B* **103**, 245119 (2021).
- [35] L. Wu, S. Patankar, T. Morimoto, N. L. Nair, E. Thewalt, A. Little, J. G. Analytis, J. E. Moore, and J. Orenstein, Giant anisotropic nonlinear optical response in transition metal monophenictide Weyl semimetals, *Nature Phys* **13**, 350 (2017).
- [36] Y.-Y. Lv, J. Xu, S. Han, C. Zhang, Y. Han, J. Zhou, S.-H. Yao, X.-P. Liu, M.-H. Lu, H. Weng, Z. Xie, Y. B. Chen, J. Hu, Y.-F. Chen, and S. Zhu, High-harmonic generation in Weyl semimetal  $\beta$ -WP<sub>2</sub> crystals, *Nat Commun* **12**, 6437 (2021).
- [37] B. Lu, S. Sayyad, M. Á. Sánchez-Martínez, K. Manna, C. Felser, A. G. Grushin, and D. H. Torchinsky, Second-harmonic generation in the topological multifold semimetal RhSi, *Phys. Rev. Research* **4**, L022022 (2022).
- [38] Z. Li, Y.-Q. Jin, T. Tohyama, T. Iitaka, J.-X. Zhang, and H. Su, Second harmonic generation in the Weyl semimetal TaAs from a quantum kinetic equation, *Phys. Rev. B* **97**, 085201 (2018).
- [39] G. B. Osterhoudt, L. K. Diebel, M. J. Gray, X. Yang, J. Stanco, X. Huang, B. Shen, N. Ni, P. J. W. Moll, Y. Ran, and K. S. Burch, Colossal mid-infrared bulk photovoltaic effect in a type-I Weyl semimetal, *Nat. Mater.* **18**, 471 (2019).
- [40] J. Ahn, G.-Y. Guo, and N. Nagaosa, Low-Frequency Divergence and Quantum Geometry of the Bulk Photovoltaic Effect in Topological Semimetals, *Phys. Rev. X* **10**, 041041 (2020).
- [41] R. P. Tiwari, B. Birajdar, and R. K. Ghosh, First-principles calculation of shift current bulk photovoltaic effect in two-dimensional  $\alpha$ -In<sub>2</sub>S<sub>3</sub>, *Phys. Rev. B* **101**, 235448 (2020).
- [42] F. De Juan, Y. Zhang, T. Morimoto, Y. Sun, J. E. Moore, and A. G. Grushin, Difference frequency generation in topological semimetals, *Phys. Rev. Research* **2**, 012017 (2020).

- [43] Z. Ni, K. Wang, Y. Zhang, O. Pozo, B. Xu, X. Han, K. Manna, J. Paglione, C. Felser, A. G. Grushin, F. De Juan, E. J. Mele, and L. Wu, Giant topological longitudinal circular photo-galvanic effect in the chiral multifold semimetal CoSi, *Nat Commun* **12**, 154 (2021).
- [44] Z. Ni, B. Xu, M.-Á. Sánchez-Martínez, Y. Zhang, K. Manna, C. Bernhard, J. W. F. Venderbos, F. De Juan, C. Felser, A. G. Grushin, and L. Wu, Linear and nonlinear optical responses in the chiral multifold semimetal RhSi, *npj Quantum Mater.* **5**, 96 (2020).
- [45] F. Flicker, F. De Juan, B. Bradlyn, T. Morimoto, M. G. Vergniory, and A. G. Grushin, Chiral optical response of multifold fermions, *Phys. Rev. B* **98**, 155145 (2018).
- [46] D. Rees, K. Manna, B. Lu, T. Morimoto, H. Borrmann, C. Felser, J. E. Moore, D. H. Torchinsky, and J. Orenstein, Helicity-dependent photocurrents in the chiral Weyl semimetal RhSi, *Sci. Adv.* **6**, eaba0509 (2020).
- [47] A. M. Cook, B. M. Fregoso, F. De Juan, S. Coh, and J. E. Moore, Design principles for shift current photovoltaics, *Nat Commun* **8**, 14176 (2017).
- [48] L. Z. Tan, F. Zheng, S. M. Young, F. Wang, S. Liu, and A. M. Rappe, Shift current bulk photovoltaic effect in polar materials—hybrid and oxide perovskites and beyond, *npj Comput Mater* **2**, 16026 (2016).
- [49] V. I. Belinicher and B. I. Sturman, The photogalvanic effect in media lacking a center of symmetry, *Sov. Phys. Usp.* **23**, 199 (1980).
- [50] V. Asnin, A. Bakun, A. Danishevskii, E. Ivchenko, G. Pikus, and A. Rogachev, “Circular” photogalvanic effect in optically active crystals, *Solid State Communications* **30**, 565 (1979).
- [51] G. E. Pikus and E. L. Ivchenko, Photogalvanic effects in noncentrosymmetric semiconductors, in *Narrow Gap Semiconductors Physics and Applications*, Vol. 133, edited by J. Ehlers, K. Hepp, R. Kippenhahn, H. A. Weidenmüller, J. Zittartz, W. Beiglböck, and W. Zawadzki (Springer Berlin Heidelberg, Berlin, Heidelberg, 1980) pp. 388–406.
- [52] H.-Y. Yang, B. Singh, J. Gaudet, B. Lu, C.-Y. Huang, W.-C. Chiu, S.-M. Huang, B. Wang, F. Bahrami, B. Xu, J. Franklin, I. Sochnikov, D. E. Graf, G. Xu, Y. Zhao, C. M. Hoffman, H. Lin, D. H. Torchinsky, C. L. Broholm, A. Bansil, and F. Tafti, Noncollinear ferromagnetic Weyl semimetal with anisotropic anomalous Hall effect, *Phys. Rev. B* **103**, 115143 (2021).
- [53] M. S. Alam, A. Fakhredine, M. Ahmad, P. K. Tanwar, H.-Y. Yang, F. Tafti, G. Cuono, R. Islam, B. Singh, A. Lynnyk, C. Autieri, and M. Matusiak, Sign change of anomalous Hall effect and anomalous Nernst effect in the Weyl semimetal CeAlSi, *Phys. Rev. B* **107**, 085102 (2023).
- [54] M. M. Piva, J. C. Souza, V. Brousseau-Couture, S. Sorn, K. R. Pakuszewski, J. K. John, C. Adriano, M. Côté, P. G. Pagliuso, A. Paramekanti, and M. Nicklas, Topological features in the ferromagnetic Weyl semimetal CeAlSi: Role of domain walls, *Phys. Rev. Research* **5**, 013068 (2023).
- [55] A. P. Sakhya, C.-Y. Huang, G. Dhakal, X.-J. Gao, S. Regmi, B. Wang, W. Wen, R.-H. He, X. Yao, R. Smith, M. Sprague, S. Gao, B. Singh, H. Lin, S.-Y. Xu, F. Tafti, A. Bansil, and M. Neupane, Observation of Fermi arcs and Weyl nodes in a noncentrosymmetric magnetic Weyl semimetal, *Phys. Rev. Materials* **7**, L051202 (2023).
- [56] N. Zhang, X. Ding, F. Zhan, H. Li, H. Li, K. Tang, Y. Qian, S. Pan, X. Xiao, J. Zhang, R. Wang, Z. Xiang, and X. Chen, Temperature-dependent and magnetism-controlled Fermi surface changes in magnetic Weyl semimetals, *Phys. Rev. Research* **5**, L022013 (2023).
- [57] Y. Zhang, H. Ishizuka, J. Van Den Brink, C. Felser, B. Yan, and N. Nagaosa, Photogalvanic effect in Weyl semimetals from first principles, *Phys. Rev. B* **97**, 241118 (2018).
- [58] F. De Juan, A. G. Grushin, T. Morimoto, and J. E. Moore, Quantized circular photogalvanic effect in Weyl semimetals, *Nat Commun* **8**, 15995 (2017).
- [59] C. Le, Y. Zhang, C. Felser, and Y. Sun, *Ab Initio* study of quantized circular photogalvanic effect in chiral multifold semimetals, *Phys. Rev. B* **102**, 121111 (2020).
- [60] G. Chang, B. Singh, S.-Y. Xu, G. Bian, S.-M. Huang, C.-H. Hsu, I. Belopolski, N. Alidoust, D. S. Sanchez, H. Zheng, H. Lu, X. Zhang, Y. Bian, T.-R. Chang, H.-T. Jeng, A. Bansil, H. Hsu, S. Jia, T. Neupert, H. Lin, and M. Z. Hasan, Magnetic and noncentrosymmetric Weyl fermion semimetals in the R AlGe family of compounds ( R = rare earth ), *Phys. Rev. B* **97**, 041104 (2018).
- [61] S.-Y. Xu, N. Alidoust, G. Chang, H. Lu, B. Singh, I. Belopolski, D. S. Sanchez, X. Zhang, G. Bian, H. Zheng, M.-A. Husanu, Y. Bian, S.-M. Huang, C.-H. Hsu, T.-R. Chang, H.-T. Jeng, A. Bansil, T. Neupert, V. N. Strocov, H. Lin, S. Jia, and M. Z. Hasan, Discovery of Lorentz-violating type II Weyl fermions in LaAlGe, *Sci. Adv.* **3**, e1603266 (2017).
- [62] G. Kresse and J. Furthmüller, Efficient iterative schemes for *ab initio* total-energy calculations using a plane-wave basis set, *Phys. Rev. B* **54**, 11169 (1996).
- [63] J. P. Perdew, K. Burke, and M. Ernzerhof, Generalized Gradient Approximation Made Simple, *Phys. Rev. Lett.* **77**, 3865 (1996).
- [64] S. L. Dudarev, G. A. Botton, S. Y. Savrasov, C. J. Humphreys, and A. P. Sutton, Electron-energy-loss spectra and the structural stability of nickel oxide: An LSDA+U study, *Phys. Rev. B* **57**, 1505 (1998).
- [65] G. Pizzi, V. Vitale, R. Arita, S. Blügel, F. Freimuth, G. Géranton, M. Gibertini, D. Gresch, C. Johnson, T. Koretsune, J. Ibañez-Azpiroz, H. Lee, J.-M. Lihm, D. Marchand, A. Marrazzo, Y. Mokrousov, J. I. Mustafa, Y. Nohara, Y. Nomura, L. Paulatto, S. Poncè, T. Ponweiser, J. Qiao, F. Thöle, S. S. Tsirkin, M. Wierzbowska, N. Marzari, D. Vanderbilt, I. Souza, A. A. Mostofi, and J. R. Yates, Wannier90 as a community code: New features and applications, *J. Phys.: Condens. Matter* **32**, 165902 (2020).
- [66] D. Gresch, Q. Wu, G. W. Winkler, R. Häuselmann, M. Troyer, and A. A. Soluyanov, Automated construction of symmetrized Wannier-like tight-binding models from *ab initio* calculations, *Phys. Rev. Materials* **2**, 103805 (2018).
- [67] S. S. Tsirkin, High performance Wannier interpolation of Berry curvature and related quantities with WannierBerri code, *npj Comput Mater* **7**, 33 (2021).
- [68] J. E. Sipe and A. I. Shkrebtii, Second-order optical response in semiconductors, *Phys. Rev. B* **61**, 5337 (2000).
- [69] R. W. Boyd, *Nonlinear Optics*, fourth edition ed. (Elsevier, AP Academic Press, London, 2020).